


**Please cite the Published Version**

Hellstern, Thomas R, Nielander, Adam C, Chakthranont, Pongkarn, King, Laurie A , Willis, Joshua J, Xu, Shicheng, MacIsaac, Callisto, Hahn, Christopher, Bent, Stacey F, Prinz, Fritz B and Jaramillo, Thomas F (2019) Nanostructuring Strategies To Increase the Photoelectrochemical Water Splitting Activity of Silicon Photocathodes. ACS Applied Nano Materials, 2 (1). pp. 6-11. ISSN 2574-0970

**DOI:** <https://doi.org/10.1021/acsanm.8b01966>

**Publisher:** American Chemical Society (ACS)

**Version:** Accepted Version

**Downloaded from:** <https://e-space.mmu.ac.uk/624297/>

**Usage rights:**  In Copyright

**Additional Information:** This is an Author Accepted Manuscript of an article published in ACS Applied Nano Materials by ACS.

**Enquiries:**

If you have questions about this document, contact [openresearch@mmu.ac.uk](mailto:openresearch@mmu.ac.uk). Please include the URL of the record in e-space. If you believe that your, or a third party's rights have been compromised through this document please see our Take Down policy (available from <https://www.mmu.ac.uk/library/using-the-library/policies-and-guidelines>)

# Nanostructuring Strategies to Increase the Photoelectrochemical Water Splitting Activity of Silicon Photocathodes

Thomas R. Hellstern\*, Adam C. Nielander\*, Pongkarn Chakthranont\*, Laurie A. King, Joshua J. Willis, Shicheng Xu, Callisto MacIsaac, Christopher Hahn, Stacey F. Bent, Fritz B. Prinz, and Thomas F. Jaramillo<sup>†</sup>

\* These authors contributed equally to this work

<sup>†</sup> Corresponding author: [jaramillo@stanford.edu](mailto:jaramillo@stanford.edu)

Dr. T.R. Hellstern, Dr. A.C. Nielander, Dr. P. Chakthranont, Dr. L.A. King, Dr. J.J. Willis, C. MacIsaac, Dr. C. Hahn, Prof. S.F. Bent, Prof. T.F. Jaramillo  
Department of Chemical Engineering, Stanford University  
443 Via Ortega, Stanford, California 94305, United States

Dr. P. Chakthranont  
Nanomaterials for Energy and Catalysis Laboratory, National Nanotechnology Center  
(NANOTEC), National Science and Technology Development Agency (NSTDA), 111 Thailand  
Science Park, Pathum Thani 12120, Thailand

Dr. S. Xu, Prof. F.B. Prinz  
Department of Mechanical Engineering, Stanford University  
443 Via Ortega, Stanford, California 94305, United States

Prof. F.B. Prinz  
Department of Material Science and Engineering, Stanford University  
443 Via Ortega, Stanford, California 94305, United States

KEYWORDS: Photoelectrochemical water splitting, molybdenum disulfide, hydrogen evolution, silicon nanowires, zinc oxide nanowires, photocathodes

ABSTRACT: Photoelectrochemical water splitting is a promising route for sustainable hydrogen production. Herein, we demonstrate a photoelectrode motif which enables a nanostructured high surface area electrocatalyst without requiring a nanostructured semiconductor surface with the goal of promoting electrocatalysis while minimizing surface recombination. We compare the photoelectrochemical H<sub>2</sub> evolution activity of two silicon photocathode nanostructuring strategies; (1) direct nanostructuring of the silicon surface, and (2) incorporation of nanostructured zinc oxide to increase electrocatalyst surface area on planar silicon. We observed silicon photocathodes which utilized nanostructured ZnO supports outperformed nanostructured silicon electrodes by ~50 mV at open-circuit under 1-sun illumination and demonstrated comparable electrocatalytic activity.

Photoelectrochemical (PEC) devices offer a unique route to sustainable, CO<sub>2</sub>-free, hydrogen generation.<sup>1</sup> A key challenge in the development of H<sub>2</sub>-generating photoelectrochemical devices is the effective integration of active hydrogen evolving electrocatalysts with light absorbing semiconductors capable of efficiently utilizing the solar spectrum.<sup>2</sup> Considering a tandem PEC device structure in which catalyst and semiconductor layers are stacked in series with respect to incoming light, the ideal photocathode electrocatalyst|semiconductor pairing must meet three requirements: 1) The electrocatalyst must be highly active toward the hydrogen evolution reaction (HER), 2) the electrocatalyst must be transparent toward the light that must pass through it to be absorbed by an underlying semiconductor, and 3) deleterious charge recombination at the electrocatalyst|semiconductor interface must be minimized.

Platinum is a highly active HER electrocatalyst and has been employed in H<sub>2</sub> generating PEC devices, however, concerns over its cost and availability have motivated significant effort toward the development of alternative non-precious metal HER electrocatalysts.<sup>3,4</sup> Studies have combined silicon absorbers with a number of non-precious metal hydrogen evolution electrocatalysts, but while discoveries in earth-abundant HER electrocatalysis have helped to close the activity gap between non-precious metal and precious metal electrodes on a geometric current density basis, the improvement of non-precious metal-catalyzed photocathodes versus their precious metal-catalyzed counterparts has been less dramatic.<sup>5-8</sup> Because the electrocatalytic HER activity of Pt is significantly greater than non-precious metal HER electrocatalysts on an active site basis, the non-precious metal electrocatalysts require thicker, high surface area structured catalyst layers to match the HER activity of Pt on a geometric basis.<sup>3</sup> However, the utilization of thicker, structured catalysts, can be detrimental to photoelectrode performance, parasitically absorbing light and thus reducing electrode performance. The interplay between catalyst activity

and parasitic absorption is particularly important in the tandem PEC water splitting device motif, which requires that light pass through at least one catalyst layer.<sup>2</sup>

A variety of strategies have been pursued to maximize the catalytic activity of PEC devices. Commonly, the micro- and nanostructuring of the semiconductor surface on which the catalyst is deposited, the direct structuring of the catalyst on the absorber, or the deposition of an absorber directly on a micro- or nanostructured support material is used to promote increased catalyst surface area and concomitantly improved charge extraction efficiency due to orthogonalization of light absorption and carrier extraction.<sup>9–16</sup> However, careful consideration is required when structuring semiconductor surfaces with respect to the complex interplay between improvements in catalysis and charge extraction against deleterious increases in junction recombination as semiconductor surface area increases.<sup>17–19</sup> The ability to decouple the catalyst surface area from the semiconductor surface area is therefore valuable, particularly when the semiconductor is of sufficient electronic quality that orthogonalization of light absorption and charge collection is not necessary for improved performance. In these cases, planar absorber surface areas would be advantageous, and this is commonly the case for crystalline silicon absorbers. Strategies that have been employed to this end on planar semiconductor absorbers to synthesize highly efficiency photocathodes include deposition of catalyst ‘islands’ via photolithography, molecular beam epitaxial growth of structured interfacial layers, and the direct growth of structured catalysts.<sup>20–23</sup> Herein, we investigated and characterized a unique electrocatalyst|semiconductor decoupling strategy that used a transparent, conductive, nanostructured interfacial layer that could be simply and directly deposited on a semiconductor substrate using a wet chemical deposition technique. Specifically, MoS<sub>2</sub>-coated, nanostructured zinc oxide transparent conducting nanowire supports (ZnO<sub>NW</sub>) were fabricated on planar n<sup>+</sup>p-Si surfaces. A ZnO<sub>NW</sub> support was selected as the

interfacial decoupling material due to its transparency as well as the ease of deposition of highly structured ZnO nanowire layers on arbitrary substrates.<sup>24,25</sup> We were interested in understanding the effect of absorber surface area on photovoltage, and the use of a structured ZnO interfacial layer allowed for the decoupling of the semiconductor surface area from the catalyst surface area with the target of an exactly planar semiconductor surface and an intrinsically maximized catalyst active area. In order to deconvolute and quantify the effects of increased electrode area and semiconductor junction surface area on the electrode electrocatalytic and photovoltaic activity, the photoelectrochemical behavior of MoS<sub>2</sub>-coated ZnO<sub>NW</sub> on planar n<sup>+</sup>p-Si electrode structures were compared with MoS<sub>2</sub>-coated Si nanowire homojunction (n<sup>+</sup>p-Si<sub>NW</sub>) structures and MoS<sub>2</sub>-coated, planar n<sup>+</sup>p-Si structures as well as the analogous structures on degenerately doped n<sup>+</sup>-Si. We further compared the photoelectrochemical activity of the analogous photoactive electrodes coated with platinum in lieu of MoS<sub>2</sub> to demonstrate the variable importance of electrode structuring when using more or less active electrocatalysts.

The nanostructured electrodes were fabricated using the appropriate various combination of atomic layer deposition (ALD), dry silicon etching, and direct solution-based deposition of ZnO nanowires. These multilayer electrode structures are denoted from the top layer using the following nomenclature: Layer A|Layer B|Layer C, etc. As an example, the MoS<sub>2</sub>|TiO<sub>2</sub>|n<sup>+</sup>p-Si<sub>NW</sub> electrode structure was composed of layers as seen in **Figure 1a** and was fabricated by sequential ALD deposition of TiO<sub>2</sub> followed by MoS<sub>2</sub> onto a prepared n<sup>+</sup>p-Si<sub>NW</sub> surface. An MoS<sub>2</sub>|TiO<sub>2</sub>|ZnO<sub>NW</sub>|Si electrode structure is depicted in **Figure 1c** and was fabricated by solution-based ZnO<sub>NW</sub> deposition followed by sequential ALD deposition of TiO<sub>2</sub> and MoS<sub>2</sub>. A complete description of the experimental details can be found in the SI, including a scheme detailing the fabrication of the electrode structures (**Figure S1**).

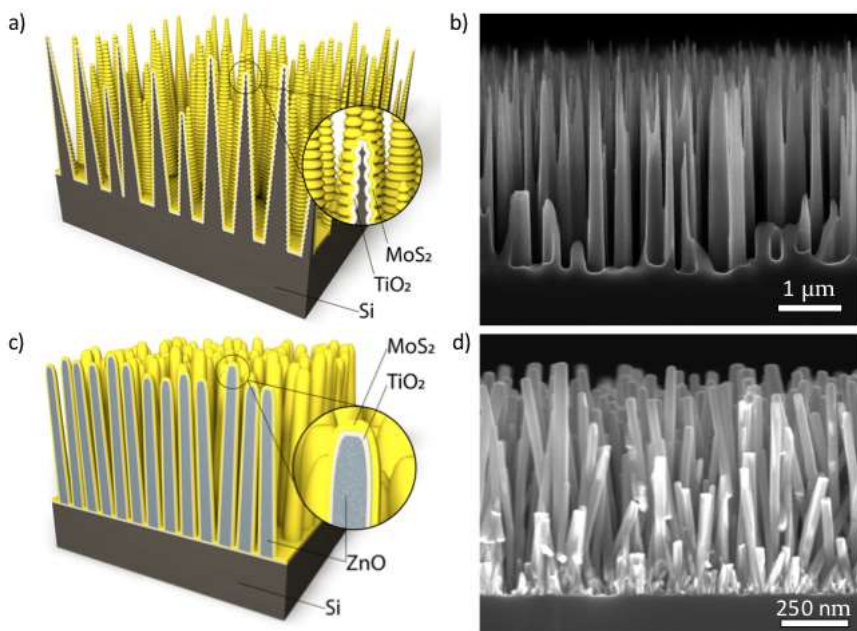


**Figure 1:** a) Schematic diagram of the  $\text{MoS}_2|\text{TiO}_2|\text{Si}_{\text{NW}}$  electrode architecture which shows the scallops resulting from the etching process. (b) cross-sectional SEM image of the  $\text{MoS}_2|\text{TiO}_2|\text{Si}_{\text{NW}}$  structure (c) Schematic diagram of  $\text{MoS}_2|\text{TiO}_2|\text{ZnO}_{\text{NW}}|\text{Si}$  electrode architecture showing vertically aligned ZnO nanowires. (d) cross-sectional SEM image of the  $\text{MoS}_2|\text{TiO}_2|\text{ZnO}_{\text{NW}}|\text{Si}$  structure.

SEM was used to characterize the morphology of the synthesized  $\text{Si}_{\text{NW}}$  and  $\text{ZnO}_{\text{NW}}$  electrodes coated with  $\text{MoS}_2$ . **Figure 1b** shows an SEM image of the  $\text{MoS}_2|\text{TiO}_2|\text{Si}_{\text{NW}}$  structure with wire lengths of  $\sim 3 \mu\text{m}$  and width  $\sim 0.3 \mu\text{m}$ . **Figure 1d** shows an SEM image of the  $\text{MoS}_2|\text{TiO}_2|\text{ZnO}_{\text{NW}}|\text{Si}$  structure with wire lengths of  $\sim 0.9 \mu\text{m}$  and widths of  $\sim 0.05 \mu\text{m}$ .  $\text{Si}_{\text{NW}}$  and  $\text{ZnO}_{\text{NW}}$  structures with length wires of  $\sim 1.5 \mu\text{m}$  and  $\sim 0.5 \mu\text{m}$ , respectively, were also synthesized and are shown in **Figure S2**. These wire lengths were selected to attempt to match catalytic activity and total surface area between the various electrode structures (see SI **Figure S3-S5**).

To probe the elemental distribution across the core-shell  $\text{MoS}_2|\text{TiO}_2|\text{ZnO}_{\text{NW}}$  architecture, STEM-EDS maps were generated and are presented in **Figure 2**. The map combining Mo, Ti, and Zn is consistent with the Mo and Ti being localized on the edges of the wire while the Zn is

confined to the core of the wire. Note that the Mo and S  $K\alpha$  lines overlap, so the Mo signal also includes the S signal. STEM-EDS maps of the  $\text{MoS}_2|\text{TiO}_2|\text{Si}_{\text{NW}}$  structure are shown in **Figure S6** and indicate an analogous core-shell elemental distribution. The deposition and loading of Pt on both  $n^+\text{-Si}$  and  $n^+\text{-Si}_{\text{NW}}$  substrates were characterized via SEM (see **Figure S7**).

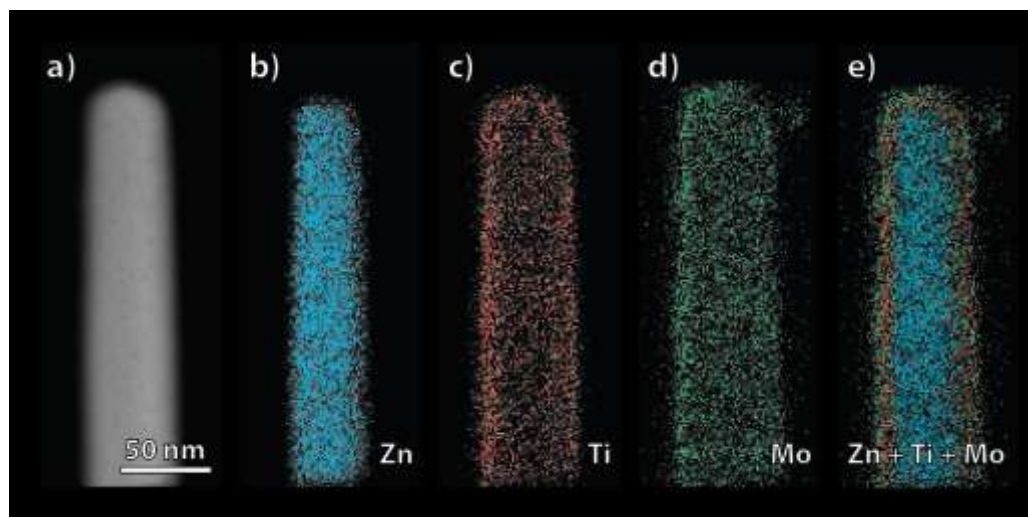


**Figure 2:** STEM image and associated EDS maps of the Mo, Ti, and Zn  $K\alpha$  regions of the  $\text{MoS}_2|\text{TiO}_2|\text{ZnONW}$  structure. (a) STEM image of nanowire. (b-d) Individual Zn, Ti, Mo EDS maps. (e) combined Zn, Ti, Mo EDS map.

The photoelectrochemical behavior of structured  $\text{MoS}_2|\text{TiO}_2|n^+\text{p-Si}_{\text{NW-3}\mu\text{m}}$ ,  $\text{MoS}_2|\text{TiO}_2|\text{ZnONW-0.9}\mu\text{m}|n^+\text{p-Si}$ , and  $\text{Pt}|\text{TiO}_2|n^+\text{p-Si}_{\text{NW-3}\mu\text{m}}$  photocathodes as well as planar  $\text{MoS}_2|\text{TiO}_2|n^+\text{p-Si}$  and  $\text{Pt}|\text{TiO}_2|n^+\text{p-Si}$  photocathodes were evaluated via LSV as seen in **Figure 3**. Additionally, intermediate length  $\text{ZnONW}$  and  $\text{Si}_{\text{NW}}$  structures were fabricated and characterized ( $\text{ZnONW-0.5}\mu\text{m}$  and  $\text{Si}_{\text{NW-1.5}\mu\text{m}}$ , SI **Figure S8**). The J-V behavior of these photocathodes was stable over the course of these measurements (See SI **Figure S9-S10**) and values for the maximum photocurrent and potential to achieve  $-10 \text{ mA cm}^{-2}$  [ $V_{\text{PEC}}(-10 \text{ mA cm}^{-2})$ ] are listed in **Table 1**. The value of  $-10 \text{ mA cm}^{-2}$  was selected as none of the electrodes were in a light-limited regime at this



current density and thus it can serve as a simple quantitative figure of merit of photoelectrode activity. The electrochemical characterization of the analogous structured electrodes on degenerately doped silicon substrates (e.g.  $\text{MoS}_2|\text{TiO}_2|\text{ZnO}_{\text{NW-0.9}\mu\text{m}}|\text{n}^+\text{-Si}$ ) was also performed (See SI **Figure S3** and **Table S1**).

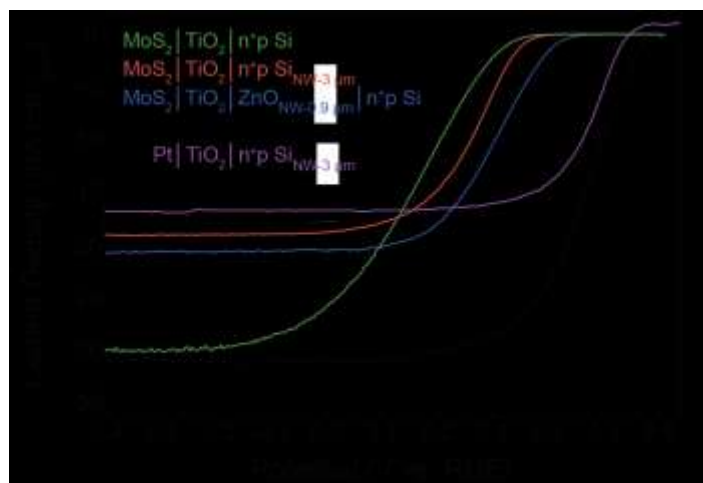


**Figure 3:** Linear sweep voltammograms of various photoelectrodes in contact with 0.5M  $\text{H}_2\text{SO}_4$ ,  $\text{H}_2$ -purged electrolyte (Sweep rate  $10 \text{ mV s}^{-1}$ , negative going scan direction) under approximately one sun illumination.

**Table 1:** Maximum photocurrent densities and potential required to achieve  $-10 \text{ mA cm}^{-2}$  [ $V_{\text{PEC}}(-10 \text{ mA cm}^{-2})$ ] for various photoelectrode architectures (see **Figure 3**).

| Electrode Structure  | Max Photocurrent density ( $\text{mA cm}^{-2}$ ) | [ $V_{\text{PEC}}(-10 \text{ mA cm}^{-2})$ ] (V vs. RHE) |
|--|--|--|
| $\text{MoS}_2 \text{TiO}_2 \text{n}^+\text{p-Si}$                              | -30  | +0.207 V   |
| $\text{MoS}_2 \text{TiO}_2 \text{n}^+\text{p-Si}_{\text{NW-3um}}$              | -19  | +0.264 V   |
| $\text{MoS}_2 \text{TiO}_2 \text{ZnO}_{\text{NW-0.9um}} \text{n}^+\text{p-Si}$ | -21  | +0.307 V   |
| $\text{Pt} \text{TiO}_2 \text{n}^+\text{p-Si}$                                 | -31  | +0.504 V   |
| $\text{Pt} \text{TiO}_2 \text{n}^+\text{p-Si}_{\text{NW-3um}}$                 | -17  | +0.465 V   |

The varying  $V_{\text{PEC}}(-10 \text{ mA cm}^{-2})$  potential of the electrodes displayed in **Figure 3** and **Table 1** were analyzed by modeling the current-voltage behavior of each photocathode as a photovoltaic

element in series with an independently operating impedance element representing the electrocatalyst behavior.<sup>26–28</sup> This assumption allows the differences in J-V behavior between two photocathodes to be assigned to their respective differences in catalytic activity and photovoltaic behavior as described in **Equation 1**.

$$V_{PEC}(J) = V_{PV}(J) + V_{cat}(J) \quad (1)$$

where  $V_{PV}(J)$ ,  $V_{cat}(J)$ , and  $V_{PEC}(J)$  represent the potential difference as a function of current density across the photovoltaic element, the electrocatalyst interface, and the photoelectrode, respectively (all values appropriately signed, usually resulting in a reduced absolute  $V_{PEC}$  value with respect to  $V_{PV}$ ). Following this assumption, for each MoS<sub>2</sub>-coated structure,  $V_{PEC}(J)$  data in **Figure 3** and  $V_{cat}(J)$  data in **Figure S3** was used to calculate  $V_{PV}(J)$  (See **Figure 4**).

The planar MoS<sub>2</sub>|TiO<sub>2</sub>|n<sup>+</sup>p-Si electrode structure demonstrated a potential to achieve -10 mA cm<sup>-2</sup> [ $V_{PEC}(-10 \text{ mA cm}^{-2})$ ] of +0.207 V vs. RHE, in line with previously synthesized MoS<sub>2</sub>-coated silicon photocathodes.<sup>6,29</sup> The Pt|TiO<sub>2</sub>|n<sup>+</sup>p-Si structure, in contrast, demonstrated a  $V_{PEC}(-10 \text{ mA cm}^{-2})$  potential of +0.504 V vs. RHE. This nearly 300 mV difference between the  $V_{PEC}(-10 \text{ mA cm}^{-2})$  potentials is consistent with the 295 mV difference in the  $V_{cat}(-10 \text{ mA cm}^{-2})$  potential between the analogous structures on n<sup>+</sup>-Si substrates (**Figure S3** and **Table S1**). This suggests that the variation in  $V_{PEC}(-10 \text{ mA cm}^{-2})$  potential is attributable to variances in catalytic activity ( $V_{cat}$ ) only and that the photovoltage ( $V_{PV}$ ) produced by the n<sup>+</sup>p-Si absorber is approximately equal in both devices (See **Figure 4** and **Figure S11**). Conversely, the potential at which the planar MoS<sub>2</sub>|TiO<sub>2</sub>|n<sup>+</sup>p-Si achieved -10 mA cm<sup>-2</sup> (+0.207 V vs. RHE) was ~60 mV more negative than for the MoS<sub>2</sub>|TiO<sub>2</sub>|n<sup>+</sup>p-Si<sub>NW-3um</sub> (+0.264 V vs. RHE). This is less than the ~120 mV difference that would have been expected if the difference in  $V_{PEC}(-10 \text{ mA cm}^{-2})$  was entirely accounted for by the

variances in catalytic activity observed in **Figure S3**, suggesting that the difference in  $V_{\text{PEC}}(-10 \text{ mA cm}^{-2})$  must additionally be the result of differences in photovoltage generated at the  $\text{n}^+\text{p-Si}$  and  $\text{n}^+\text{p-Si}_{\text{NW-3}\mu\text{m}}$  junctions. The lower photocurrent density observed for the  $\text{MoS}_2|\text{TiO}_2|\text{n}^+\text{p-Si}_{\text{NW}}$  structure relative to the  $\text{MoS}_2|\text{TiO}_2|\text{n}^+\text{p-Si}$ , which we attribute to differences in light absorption and scattering from planar and structured surfaces (**Figure S12**, see SI for extended discussion), should account for  $\sim 10 \text{ mV}$  of the difference based as dictated by the ideal diode equation, (See SI, **Equation S1**). The remainder of the difference between the flat  $\text{MoS}_2|\text{TiO}_2|\text{n}^+\text{p-Si}$  and the nanostructured  $\text{MoS}_2|\text{TiO}_2|\text{n}^+\text{p-Si}_{\text{NW-3}\mu\text{m}}$   $V_{\text{PEC}}(-10 \text{ mA cm}^{-2})$  potentials ( $\sim 60 \text{ mV}$ ) is therefore attributed to a higher saturation current density associated with the  $\text{n}^+\text{p-Si}_{\text{NW-3}\mu\text{m}}$  junction relative to the  $\text{n}^+\text{p-Si}$  junction, which manifests in **Figure 4** as a reduced open-circuit voltage [ $V_{\text{PV}}(0 \text{ mA cm}^{-2})$ ]. The reduced open-circuit voltage associated with the  $\text{n}^+\text{p-Si}_{\text{NW}}$  junction is consistent with a larger contribution from surface recombination for the high surface roughness  $\text{n}^+\text{p-Si}_{\text{NW-3}\mu\text{m}}$  junction than the planar  $\text{n}^+\text{p-Si}$  junction. An explanation of the origins of increased surface recombination is presented in **Figure S13**.<sup>30,31</sup> The relationship between increased absorber surface roughness and increased carrier recombination is further supported by the photoelectrochemical behavior of the intermediate length nanowire  $\text{MoS}_2|\text{TiO}_2|\text{n}^+\text{p-Si}_{\text{NW-1.5}\mu\text{m}}$  structure, which displayed an intermediate open-circuit voltage with respect to the planar and  $3 \mu\text{m}$  length nanowire structures. The fill factors observed in **Figure 4** ( $\text{ff} > 0.5$ ) and the low measured series resistances for the various photoactive and degenerately doped electrode architectures ( $15\text{-}30 \Omega$ , See SI and **Figure 3** and **Figure S3**) were consistent with low resistance ohmic contacts between the layers of the electrode structure, including the Si/ZnO interface.

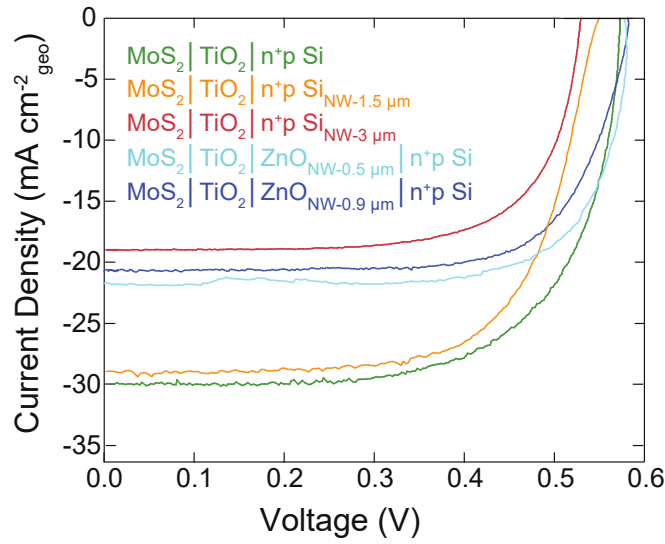


**Figure 4:**  $V_{PV}(J)$  plotted with current density as a function of voltage for  $\text{MoS}_2|\text{TiO}_2|\text{n}^+\text{p-Si}$  (green),  $\text{MoS}_2|\text{TiO}_2|\text{n}^+\text{p-Si}_{\text{NW-1.5}\mu\text{m}}$  (orange),  $\text{MoS}_2|\text{TiO}_2|\text{n}^+\text{p-Si}_{\text{NW-3}\mu\text{m}}$  (red),  $\text{MoS}_2|\text{TiO}_2|\text{ZnO}_{\text{NW-0.5}\mu\text{m}}|\text{n}^+\text{p-Si}$  (light blue), and  $\text{MoS}_2|\text{TiO}_2|\text{ZnO}_{\text{NW-0.9}\mu\text{m}}|\text{n}^+\text{p-Si}$  (dark blue).

**Table 2:** Potential to achieve  $-10 \text{ mA cm}^{-2}$  [ $V_{\text{PEC}}(-10 \text{ mA cm}^{-2})$ ] and open-circuit potentials [ $V_{\text{PV}}(0 \text{ mA cm}^{-2})$ ] for various  $\text{MoS}_2$ -coated photoelectrode architectures (see **Figure 4**).

| Electrode Structure   | $V_{\text{PEC}}(-10 \text{ mA cm}^{-2})$ (V vs. RHE) | $V_{\text{pv}}(0 \text{ mA cm}^{-2})$ (V)<br>[Open-Circuit Voltage] |
|---|--|---|
| $\text{MoS}_2 \text{TiO}_2 \text{n}^+\text{p-Si}$                                       | +0.207   | +0.572  |
| $\text{MoS}_2 \text{TiO}_2 \text{n}^+\text{p-Si}_{\text{NW-3}\mu\text{m}}$              | +0.264   | +0.530  |
| $\text{MoS}_2 \text{TiO}_2 \text{ZnO}_{\text{NW-0.9}\mu\text{m}} \text{n}^+\text{p-Si}$ | +0.307   | +0.580  |
| $\text{MoS}_2 \text{TiO}_2 \text{n}^+\text{p-Si}_{\text{NW-1.5}\mu\text{m}}$            | +0.242   | +0.550  |
| $\text{MoS}_2 \text{TiO}_2 \text{ZnO}_{\text{NW-0.5}\mu\text{m}} \text{n}^+\text{p-Si}$ | +0.283   | +0.576  |

In contrast to the MoS<sub>2</sub>-coated Si<sub>NW</sub> electrodes, the nanostructured ZnO<sub>NW</sub> on planar n<sup>+</sup>p-Si electrodes displayed V<sub>PEC</sub>(-10 mA cm<sup>-2</sup>) potential differences which can be accounted for almost entirely by differences in the catalytic activity of the structures. This can be observed in **Figure 4** and **Table 2** as the clustering of open-circuit potentials for the planar n<sup>+</sup>p-Si structures to a <10 mV range between 570-580 mV. The observed small voltage deviations are likely a result of differences in the number of photons absorbed in the silicon, small variations in the semiconductor junction quality, or small morphological variance between the synthesized ZnO nanowires.

The photoelectrochemical behavior of the nanostructured Si electrodes indicate a tradeoff between semiconductor junction photoactivity and catalytic activity when the silicon is nanostructured. As the Si nanowire length increases, catalytic activity increases and photoactivity decreases with a maximum observed open-circuit voltage loss of ~50 mV for the Si<sub>NW-3μm</sub> structure. In contrast with the Si<sub>NW</sub> electrodes, the ZnO<sub>NW</sub> on planar n<sup>+</sup>p-Si electrodes appear to have constant photoactivity in line the planar MoS<sub>2</sub>|TiO<sub>2</sub>|n<sup>+</sup>p Si electrodes while at the same time displaying improved catalytic performance as the ZnO nanowire length increases. This comparison supports the hypothesis that decoupling the catalyst structure from the semiconductor absorber structure, particularly when using electronic quality silicon absorbers, is a useful strategy to achieve earlier onsets and the lower overpotential required to achieve useful current densities. While it is important to note that the durability of these electrodes is ultimately limited by ZnO stability in strongly acidic electrolyte, the ZnO<sub>NW</sub>|Si electrodes represent an important class of device structure that can be synthesized with a variety of transparent conducting oxide materials in order to stably achieve electrocatalyst|semiconductor structure decoupling in order to fabricate maximally efficient devices that employ earth abundant catalyst materials. The reduction in light

limited current density observed for the nanostructured electrodes in **Figure 3** was in contrast to the expectation that the nanostructured materials generally improve optical absorption.<sup>18</sup> This may be a result of increased absorption in the catalyst or interfacial layers, as recently demonstrated, improvements in catalyst placement and thickness are means to reduce this effect (See SI).<sup>14</sup> There is also room to develop improved combinations of electrolyte conditions and the catalyst material to maximize both the efficiency and stability of photocathodes employing conductive oxide interfaces that can be readily deposited on a range of semiconductor absorbers.

Herein, we demonstrated and quantified a strategy for the decoupling of electrocatalytic surface area from the surface structure of a photoactive silicon light absorber through the use of a zinc oxide nanowire support and facile ALD deposition of the earth abundant MoS<sub>2</sub> as an HER catalyst. Comparisons between nanostructured Si<sub>NW</sub> surfaces and ZnO<sub>NW</sub> surfaces suggested that the ZnO<sub>NW</sub> support allowed silicon photocathodes to obtain both the electrocatalytic activity of a structured catalyst while retaining the photoactivity of a planar silicon homojunction. This should be a general strategy for the use of the incorporation of earth abundant hydrogen evolution catalysts into solar fuels devices without hindering device efficiency, and additional work toward finding readily deposited, transparent nanostructures should further generalize this strategy across light absorber and electrolyte conditions.

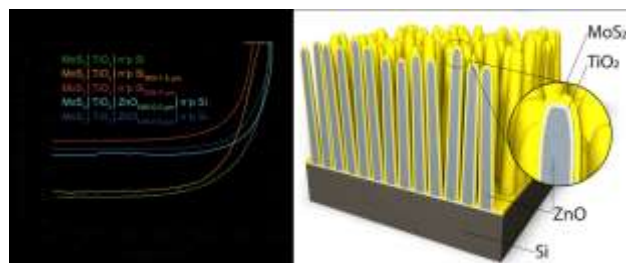
## **Acknowledgment**

The work was funded by the Department of Energy under contract no. DE-EE0006670, administrated by the University of Hawaii. Part of this work was performed at the Stanford Nano Shared Facilities (SNSF), supported by the National Science Foundation under award ECCS-1542152. Part of this work was also conducted at the Stanford Nanofabrication Facility (SNF). TRH would like to thank the National Science Foundation for its support through the Graduate Research Fellowship Program.

## Supporting Information

Detailed characterization of electrode structures via SEM, STEM-EDX, capacitance measurement, UV-Visible spectroscopy, and photoelectrochemical I-V measurements. Extended description of surface recombination in crystalline silicon devices. Full description of experimental methods.

## TOC Graphic



## References

- (1) Shaner, M. R.; Atwater, H. A.; Lewis, N. S.; McFarland, E. W. A Comparative Technoeconomic Analysis of Renewable Hydrogen Production Using Solar Energy. *Energy Environ. Sci.* **2016**, *9*, 2354–2371.
- (2) Walter, M. G.; Warren, E. L.; McKone, J. R.; Boettcher, S. W.; Mi, Q. X.; Santori, E. A.; Lewis, N. S. Solar Water Splitting Cells. *Chem. Rev.* **2010**, *110*, 6446–6473.
- (3) McCrory, C. C. L.; Jung, S.; Ferrer, I. M.; Chatman, S. M.; Peters, J. C.; Jaramillo, T. F. Benchmarking HER and OER Electrocatalysts for Solar Water Splitting Devices. *J. Am. Chem. Soc.* **2015**, *137*, 4347–4357.
- (4) Ager, J. W.; Shaner, M. R.; Walczak, K. A.; Sharp, I. D.; Ardo, S. Experimental Demonstrations of Spontaneous, Solar-Driven Photoelectrochemical Water Splitting. *Energy Environ. Sci.* **2015**, *8*, 2811–2824.

- (5) Roske, C. W.; Popczun, E. J.; Seger, B.; Read, C. G.; Pedersen, T.; Hansen, O.; Vesborg, P. C. K.; Brunenschwig, B. S.; Schaak, R. E.; Chorkendorff, I.; Gray, H. B.; Lewis, N. S. Comparison of the Performance of CoP-Coated and Pt-Coated Radial Junction N<sup>+</sup>p-Silicon Microwire-Array Photocathodes for the Sunlight-Driven Reduction of Water to H<sub>2</sub>(G). *J. Phys. Chem. Lett.* **2015**, 1679–1683.
- (6) Laursen, A. B.; Pedersen, T.; Malacrida, P.; Seger, B.; Hansen, O.; Vesborg, P. C. K.; Chorkendorff, I. MoS<sub>2</sub>-an Integrated Protective and Active Layer on n(+)p-Si for Solar H<sub>2</sub> Evolution. *Phys. Chem. Chem. Phys.* **2013**, 15, 20000–20004.
- (7) McKone, J. R.; Warren, E. L.; Bierman, M. J.; Boettcher, S. W.; Brunenschwig, B. S.; Lewis, N. S.; Gray, H. B. Evaluation of Pt, Ni, and Ni–Mo Electrocatalysts for Hydrogen Evolution on Crystalline Si Electrodes. *Energy Environ. Sci.* **2011**, 4, 3573.
- (8) Seger, B.; Laursen, A. B.; Vesborg, P. C. K.; Pedersen, T.; Hansen, O.; Dahl, S.; Chorkendorff, I. Hydrogen Production Using a Molybdenum Sulfide Catalyst on a Titanium-Protected n plus p-Silicon Photocathode. *Angew. Chemie-International Ed.* **2012**, 51, 9128–9131.
- (9) Chakthranont, P.; Pinaud, B. A.; Seitz, L. C.; Forman, A. J.; Jaramillo, T. F. Improving the Photoelectrochemical Performance of Hematite by Employing a High Surface Area Scaffold and Engineering Solid-Solid Interfaces. *Adv. Mater. Interfaces* **2016**, 3, 1500626.
- (10) Lin, Y.; Yuan, G.; Sheehan, S.; Zhou, S.; Wang, D. Hematite-Based Solar Water Splitting: Challenges and Opportunities. *Energy Environ. Sci.* **2011**, 4, 4862–4869.
- (11) Sim, U.; Jeong, H.-Y.; Yang, T.-Y.; Nam, K. T. Nanostructural Dependence of Hydrogen



- Production in Silicon Photocathodes. *J. Mater. Chem. A* **2013**, *1*, 5414.
- (12) Oh, J.; Deutsch, T. G.; Yuan, H.-C.; Branz, H. M. Nanoporous Black Silicon Photocathode for H<sub>2</sub> Production by Photoelectrochemical Water Splitting. *Energy Environ. Sci.* **2011**, *4*, 1690–1694.
- (13) Lee, M. H.; Takei, K.; Zhang, J.; Kapadia, R.; Zheng, M.; Chen, Y.-Z.; Nah, J.; Matthews, T. S.; Chueh, Y.-L.; Ager, J. W.; Javey, A. P-Type InP Nanopillar Photocathodes for Efficient Solar-Driven Hydrogen Production. *Angew. Chemie Int. Ed.* **2012**, *51*, 10760–10764.
- (14) Kempler, P. A.; Gonzalez, M. A.; Papadantonakis, K. M.; Lewis, N. S. Hydrogen Evolution with Minimal Parasitic Light Absorption by Dense Co–P Catalyst Films on Structured p-Si Photocathodes. *ACS Energy Lett.* **2018**, *3*, 612–617.
- (15) Morales-Guio, C. G.; Mayer, M. T.; Yella, A.; Tilley, S. D.; Grätzel, M.; Hu, X. An Optically Transparent Iron Nickel Oxide Catalyst for Solar Water Splitting. *J. Am. Chem. Soc.* **2015**, *137*, 9927–9936.
- (16) Ding, Q.; Zhai, J.; Cabán-Acevedo, M.; Shearer, M. J.; Li, L.; Chang, H. C.; Tsai, M. L.; Ma, D.; Zhang, X.; Hamers, R. J.; He, J. H.; Jin, S. Designing Efficient Solar-Driven Hydrogen Evolution Photocathodes Using Semitransparent MoQ<sub>x</sub>Cly (Q = S, Se) Catalysts on Si Micropyramids. *Adv. Mater.* **2015**, *27*, 6511–6518.
- (17) Kayes, B. M.; Atwater, H. A.; Lewis, N. S. Comparison of the Device Physics Principles of Planar and Radial P-n Junction Nanorod Solar Cells. *J. Appl. Phys.* **2005**, *97*.
- (18) Warren, E. L.; Atwater, H. A.; Lewis, N. S. Silicon Microwire Arrays for Solar Energy-

- Conversion Applications. *J. Phys. Chem. C* **2014**, *118*, 747–759.
- (19) Garnett, E. C.; Yang, P.; Garnett, E. C.; Yang, P. Silicon Nanowire Radial p - n Junction Solar Cells Silicon Nanowire Radial p - n Junction Solar Cells. **2008**, *130*, 9224–9225.
- (20) Sun, K.; Ritzert, N. L.; John, J.; Tan, H.; Hale, W. G.; Jiang, J.; Moreno-Hernandez, I.; Papadantonakis, K. M.; Moffat, T. P.; Brunschwig, B. S.; Lewis, N. S. Performance and Failure Modes of Si Anodes Patterned with Thin-Film Ni Catalyst Islands for Water Oxidation. *Sustain. Energy Fuels* **2018**, 983–998.
- (21) Oh, S.; Song, H.; Oh, J. An Optically and Electrochemically Decoupled Monolithic Photoelectrochemical Cell for High-Performance Solar-Driven Water Splitting. *Nano Lett.* **2017**, *17*, 5416–5422.
- (22) Fan, R.; Mao, J.; Yin, Z.; Jie, J.; Dong, W.; Fang, L.; Zheng, F.; Shen, M. Efficient and Stable Silicon Photocathodes Coated with Vertically Standing Nano-MoS<sub>2</sub> Films for Solar Hydrogen Production. *ACS Appl. Mater. Interfaces* **2017**, *9*, 6123–6129.
- (23) Zhou, B.; Kong, X.; Vanka, S.; Chu, S.; Ghamari, P.; Wang, Y.; Pant, N.; Shih, I.; Guo, H.; Mi, Z. Gallium Nitride Nanowire as a Linker of Molybdenum Sulfides and Silicon for Photoelectrocatalytic Water Splitting. *Nat. Commun.* **2018**, *9*.
- (24) Greene, L. E.; Law, M.; Tan, D. H.; Montano, M.; Goldberger, J.; Somorjai, G.; Yang, P. General Route to Vertical ZnO Nanowire Arrays Using Textured ZnO Seeds. *Nano Lett.* **2005**, *5*, 1231–1236.
- (25) Srikant, V.; Clarke, D. R. On the Optical Band Gap of Zinc Oxide. *J. Appl. Phys.* **1998**, *83*, 5447–5451.

- (26) Lin, F.; Boettcher, S. W. Adaptive Semiconductor/Electrocatalyst Junctions in Water-Splitting Photoanodes. *Nat. Mater.* **2014**, *13*, 81–86.
- (27) Coridan, R. H.; Nielander, A. C.; Francis, S. A.; McDowell, M. T.; Dix, V.; Chatman, S. M.; Lewis, N. S. Methods for Comparing the Performance of Energy-Conversion Systems for Use in Solar Fuels and Solar Electricity Generation. *Energy Environ. Sci.* **2015**, *8*, 2886–2901.
- (28) Rocheleau, R.; Miller, E. Photoelectrochemical Production of Hydrogen: Engineering Loss Analysis. *Int. J. Hydrogen Energy* **1997**, *22*, 771–782.
- (29) Benck, J. D.; Hellstern, T. R.; Kibsgaard, J.; Chakthranont, P.; Jaramillo, T. F. Catalyzing the Hydrogen Evolution Reaction (HER) with Molybdenum Sulfide Nanomaterials. *ACS Catal.* **2014**, *4*, 3957–3971.
- (30) Oh, J.; Yuan, H. C.; Branz, H. M. An 18.2%-Efficient Black-Silicon Solar Cell Achieved through Control of Carrier Recombination in Nanostructures. *Nat. Nanotechnol.* **2012**, *7*, 743–748.
- (31) Aberle, A. G. Surface Passivation of Crystalline Silicon Solar Cells: A Review. *Prog. Photovoltaics* **2000**, *8*, 473–487.